

High-Throughput Selection and Experimental Realization of Two New Ce-Based Nitride Perovskites: CeMoN₃ and CeWN₃

Rachel Sherbondy,^{*} Rebecca W. Smaha, Christopher J. Bartel, Megan E. Holtz, Kevin R. Talley, Ben Levy-Wendt, Craig L. Perkins, Serena Eley, Andriy Zakutayev,^{*} and Geoff L. Brennecke^{*}



Cite This: <https://doi.org/10.1021/acs.chemmater.2c01282>



Read Online

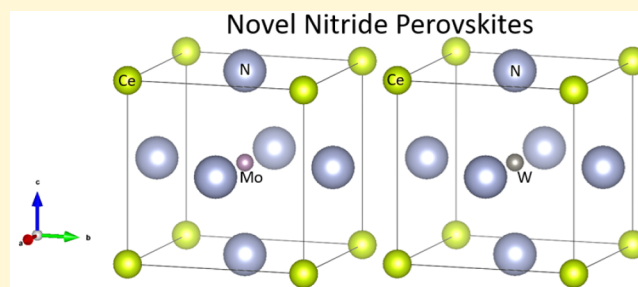
ACCESS |

Metrics & More

Article Recommendations

Supporting Information

ABSTRACT: Nitride perovskites have only been experimentally realized in very few cases despite the widespread existence and commercial importance of perovskite materials. From oxide perovskites used in ultrasonics to halide perovskites that have revolutionized the photovoltaics industry, the discovery of new perovskite materials has historically impacted a wide number of fields. Here, we add two new perovskites, CeWN₃ and CeMoN₃, to the list of experimentally realized perovskite nitrides using high-throughput computational screening and subsequent high-throughput thin film growth techniques. Candidate compositions are first down-selected using a tolerance factor and then thermochemical stability. A novel competing fluorite-family phase is identified for both material systems, which we hypothesize is a transient intermediate phase that crystallizes during the evolution from an amorphous material to a stable perovskite. Different processing routes to overcome the competing fluorite phase and obtain phase-pure nitride perovskites are demonstrated for the CeMoN_{3-x} and CeWN_{3-x} material systems, which provide a starting point for the development of future nitride perovskites. Additionally, we find that these new perovskite phases have interesting low-temperature magnetic behavior: CeMoN_{3-x} orders antiferromagnetically below $T_N \approx 8$ K with indications of strong magnetic frustration, while CeWN_{3-x} exhibits no long-range order down to $T = 2$ K but has strong antiferromagnetic correlations. This work demonstrates the importance and effectiveness of using high-throughput techniques, both computational and experimental: they are integral to optimize the process of realizing two entirely novel nitride perovskites.



INTRODUCTION

As chemists and materials scientists expand the palette of available materials, interest in new nitrides continues to grow.^{1,2} The perovskite structure, with the basic formula ABX₃, underlies the properties and function of materials crucial to fields including solar research, ultrasonics, fuel cells, and many more, but there is a notable lack of reported nitrides with the perovskite structure. A few recent computational studies have predicted the stability of rare earth transition metal nitride perovskites^{3–6} and interesting ferroic properties such as ferroelectricity in LaWN₃ and ferromagnetism in a broad range of REMN₃ (RE = rare earth; M = W, Re) compounds.^{7,8} Experimental reports are quite limited and frequently resulted instead in oxynitrides, though these too have been shown to exhibit a variety of interesting properties, from electrochemical activity to colossal magnetoresistance.^{9–15} In contrast, a number of nitrogen-containing antiperovskites have been successfully synthesized.¹⁶

The paucity of nitride perovskites reflects the difficulty of synthesizing oxygen-free phases in these systems. However, recent work from our team,¹⁷ realizing thin film perovskite LaWN₃, and from Klotz et al.,¹⁸ synthesizing bulk perovskite

LaReN₃, has paved the way for additional investigations into nitride perovskites. LaWN₃ was grown in thin film form as an oxygen-free, polar rhombohedral perovskite phase that exhibited a strong piezoelectric response;¹⁷ the use of an activated nitrogen plasma increased the chemical potential of nitrogen, which has been shown to aid the stabilization of nitrides.¹⁹ LaReN₃, which exhibits metallic conductivity and Pauli paramagnetism, was synthesized via high pressure–high temperature methods and crystallized in triclinic symmetry because of orbital ordering distortions, despite a Goldschmidt tolerance factor of 0.99, which would normally suggest cubic symmetry.¹⁸ These recent studies provide motivation and potential approaches to expand the phase space of nitride perovskites.

The present work focuses on experimental realization of new nitride perovskites in thin film form following a high-throughput materials investigation scheme, which has been successful in uncovering many new ternary nitride com-

Received: April 27, 2022

Revised: July 22, 2022

Table 1. Summary of Stability and Predicted Properties for 9 Compositions Evaluated for Viability as Nitride Perovskites^a

formula	$P(\tau)$	t	μ	ΔH_f (eV/atom)	ΔH_d (eV/atom)	E_g (eV)	E_{gd} (eV)
CeNbN ₃	1.00	0.87	0.42	−1.132	−0.086	0.63	0.63
CeTaN ₃	1.00	0.87	0.42	−1.314	−0.115	0.65	0.65
CeMoN ₃	0.98	0.96	0.38	−0.887	−0.133	metal	metal
CeWN ₃	0.98	0.95	0.39	−1.021	−0.249	metal	metal
LaMoN ₃	0.98	0.96	0.38	−0.867	−0.182	0.55	0.55
LaWN ₃	0.98	0.96	0.39	−1.011	−0.309	1.11	1.11
YMoN ₃	0.94	0.87	0.38	−0.870	−0.023	1.18	1.30
YWN ₃	0.94	0.86	0.39	−0.998	−0.135	1.07	1.18
InMoN ₃	0.55	0.82	0.38	0.212	0.368	1.00	1.02

^a $P(\tau)$ is the probability of forming the perovskite on the basis of the recently introduced tolerance factor, τ (values > 0.5 indicate perovskite). t is Goldschmidt's tolerance factor, with values between 0.8 and 1.1 usually indicating perovskite is plausible. μ is the octahedral factor, where values > 0.38 indicate the B cation can likely be coordinated by at least six anions. ΔH_f is the formation enthalpy, ΔH_d is the decomposition enthalpy, E_g is the band gap, and E_{gd} the direct band gap, all computed with PBE.³⁸

pounds.^{1,2,15,20–30} We first identify likely candidates via a computational screening process using a recent radii-based method developed by a portion of our team³¹ to predict the likelihood of each candidate forming in a perovskite structure—improving upon the Goldschmidt tolerance factor³²—followed by density functional theory (DFT) calculations to predict their stability.

Six pairs of A- and B-site cations computationally identified as likely to form stable nitride perovskites are experimentally explored in initial combinatorial thin film libraries with intentional chemical gradients to ensure the presence of a 1:1 cation ratio without the need for multiple synthesis experiments for each chemistry. Throughout this manuscript, ABN₃ refers to the ideal perovskite phase of that composition. In experimentally realized films, we use ABN_{3–x} to designate the perovskite phase with unknown anion versus cation stoichiometry. We use (A,B)N_{3–x} to refer to the overall compositionally graded films.

Two compositions, CeMoN₃ and CeWN₃, are selected for further study. Initial growths of these two compounds exhibit a mixture of phases, fluorite family and perovskite family, and we posit that the fluorite phase is an intermediate stabilized by defects and/or cation disorder. We investigate different synthetic routes for achieving phase-pure perovskite by overcoming this competing fluorite phase. This joint computational and experimental study results in the growth of two new nitride perovskites CeMoN_{3–x} and CeWN_{3–x} in thin film form, and we characterize their structure and composition as well as their low-temperature magnetic properties.

METHODS SECTION

Computational Methods. To generate a theoretical library of potential ABN₃ perovskites, we considered 39 A/B cations—Li, Na, K, Rb, Cs, Mg, Ca, Sr, Ba, Sc, Y, Ti, Zr, Hf, La, Ce, V, Nb, Ta, Cr, Mo, W, Mn, Fe, Co, Ni, Pd, Pt, Cu, Ag, Au, Zn, Al, Ga, In, C, Si, Ge, and Sn. These cations were applied combinatorially to generate 741 ABN₃ formulas. Oxidation states for each formula were assigned automatically using the approach described in ref 31. Ionic radii were then assigned for each ion using the table provided by Shannon,³³ allowing for the application of radii-based descriptors (Goldschmidt's tolerance factor, the octahedral factor, and the recently introduced tolerance factor τ ³¹). In the perovskite structure, the anion is 6-fold coordinated, but Shannon's table of effective ionic radii does not provide an ionic radius for N^{3–} in a 6-fold coordination. We therefore increased the provided 4-fold coordination radius of 1.46 Å to 1.54 Å to account for the 6-fold coordination environment using the following relation from ref 34:

$$r(\text{CN} = x) = r(\text{CN} = 6) \times (x/6)^{(1/8)} \quad (1)$$

where $x = 4$ has a known radius of 1.46 Å for N^{3–}, allowing the calculation of the radius of 1.54 Å for $x = 6$ for N^{3–}. The descriptor values are provided in Table S1 in the Supporting Information for all 189 charge-balanced ABN₃ compositions.

For all 9 of the ABN₃ compounds predicted to be stable as perovskites on the basis of the radii-based descriptors that are listed in Table 1, we used density functional theory (DFT) to support their stabilities in the perovskite structure and calculate some basic electronic properties. All DFT calculations were performed using the projector augmented wave method^{35,36} as implemented in the Vienna ab initio simulation package (VASP).³⁷ For initial calculations on these 9 compounds, we used the generalized gradient approximation (GGA) as implemented by Perdew, Burke, and Ernzerhof (PBE).³⁸ We calculated the thermodynamic stability of each phase relative to all stable compounds in each A–B–N chemical space available in the Materials Project.³⁹ Formation enthalpies, ΔH_f , were calculated using elemental reference energies computed in ref 40. Decomposition enthalpies, ΔH_d , were computed using the convex hull formalism.⁴¹ Each ABN₃ composition was initialized in $2 \times 2 \times 2$ supercells of the cubic perovskite structure with random perturbations of 0.2 Å applied to each ion to break symmetry.⁴² Geometry optimizations were performed using spin-polarized calculations with an initial high-spin ferromagnetic configuration, a plane wave energy cutoff of 520 eV, and a Γ -centered Monkhorst–Pack k-point grid with $25|b_i|$ discretizations along each reciprocal lattice vector. Additional antiferromagnetic (AFM) configurations were also sampled for orthorhombic CeMoN₃ and CeWN₃. For all calculations, electronic iterations were converged to 10^{-6} eV and ionic iterations were converged to 0.02 eV/Å.

For detailed investigations into CeMoN₃ and CeWN₃, the r2SCAN meta-GGA density functional⁴³ was used with an increased plane wave energy cutoff of 680 eV. These compounds were calculated in the cubic, orthorhombic, tetragonal, and rhombohedral perovskite symmetries, with the orthorhombic symmetry being identified as the lowest energy distortion for both chemistries. To further validate the thermodynamic stability of these two compounds, a number of binary competing phases in the Ce–N, W–N, and Mo–N chemical spaces were also calculated. In the Ce–N space, we considered cubic CeN, bixbyite Ce₂N₃, pyrochlore Ce₄N₇, and fluorite CeN_{2–x} ($x = 1/4, 1/2, 3/4, 1$). In the M–N ($M = \text{Mo}, \text{W}$) chemical spaces, we considered anatase M₂N, WC-structured MN, pernitride MN₂, and hexagonal MN_{1–x} ($x = 0, 1/8, 1/4, 3/8, 1/2$).

Synthesis Methods. Based upon these calculations, compositions of LaWN₃ (confirming earlier work),¹⁷ LaMoN₃, CeWN₃, CeMoN₃, YWN₃, and YMoN₃ were targeted for experimental screening. The initial sample libraries were synthesized using RF magnetron cosputtering from elemental metallic targets of Ce (QS Advanced Materials, 99.9%), W (Kurt J. Lesker, 99.95%), and Mo (Kurt J. Lesker, 99.95%) in a reactive nitrogen atmosphere. For each material ABN₃, a gradient of the A–B cations was intentionally grown in a

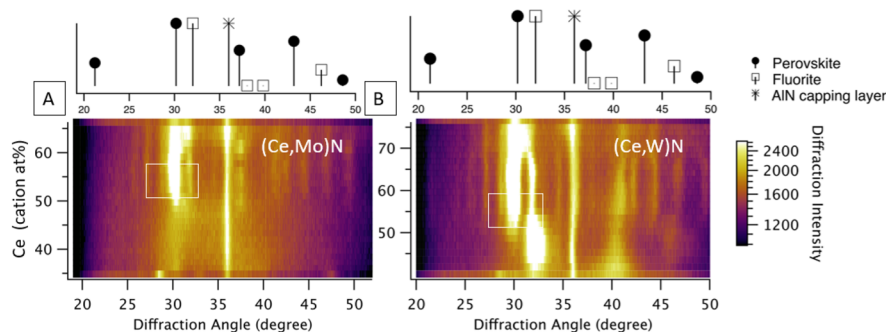


Figure 1. Lab XRD of different stoichiometries in the (Ce,Mo)N system (A) and the (Ce,W)N system (B) showing the coexisting fluorite family near the perovskite 1:1 cation ratio. The white boxes highlight the coexistence of the highest intensity perovskite and highest intensity fluorite diffraction peaks. Reference peaks are based off of the cubic prototype of the perovskite structure.

nitriding environment to observe correlations between the stoichiometry and the phases present. Deposition parameters and resulting composition gradient ranges are shown in the [Supporting Information](#), Table S2. These screening films were capped with ~ 50 nm of sputtered AlN without breaking vacuum to protect against oxidation. All initial films were grown using a nitrogen plasma with RF power of 450 W, and all were grown using a liquid nitrogen cryoshroud to minimize water vapor near the substrate. The base pressure in the chamber was between 1.8×10^{-7} and 4.5×10^{-7} Torr. All initial screening samples were annealed at 1173 K for 1 min in a ULVAC MILA-3000 rapid thermal anneal (RTA) furnace under flowing N_2 . Subsequent semiautomated, highly parallelized measurement and characterization, as described elsewhere,^{2,15,22,44–46} were performed to analyze the initial growth results.

Initial screening prioritized $CeWN_3$ and $CeMoN_3$ for further study, as discussed in the [High-Throughput Computational and Experimental Screening](#) section below. Additional $CeWN_3$ sample libraries were grown with an approximate substrate temperature of 900 K, 40 W on the W target (13 W/in²), 60 W on the Ce target (19 W/in²), a deposition time of 120 min after 70 min of presputtering (using the same powers and gas flows listed but with the sample shutter closed), a RF nitrogen plasma power of 450 W, a total chamber pressure of 4 mTorr, 8 sccm of flowing N_2 , and 4 sccm of flowing Ar. A RF substrate bias of 50 W was used in this case. This film was grown on a substrate of 100 nm LCPVD-grown SiN_x on miscut Si (University Wafers).

Additional $CeMoN_3$ films were grown after screening on p-doped Si at an approximate substrate temperature of 900 K, 35 W on the Mo target (11 W/in²), 65 W on the Ce target (21 W/in²), a deposition time of 360 min after 60 min of presputtering, no applied substrate bias, a total chamber pressure of 4 mTorr, 8 sccm of flowing N_2 , and 4 sccm of flowing Ar. $CeMoN_3$ films were treated with a RTA after growth under flowing N_2 . Heating profiles always started with a 3 min hold at 373 K followed by a 2 min ramp to 1173 K with hold times of 5 min, with successive rounds of this same treatment as listed below. The total time given is in terms of the cumulative hold times only.

Characterization Methods. Combinatorial data (lab XRD and XRF) were analyzed using the COMBIgor software package.⁴⁴ X-ray diffraction (XRD) patterns were collected using a Bruker D8 Discover with Cu $K\alpha$ radiation. LeBail fits were performed with GSAS-II.⁴⁷ Bright field transmission electron microscopy (BF TEM) images and scanning transmission electron microscopy (STEM) images were acquired on a ThermoFisher FEI Talos F200X. Cross-sectional specimens for TEM analysis were prepared using focused ion beam lift-off on a ThermoFisher FEI Helios NanoLab 600i ($CeWN$) and a TESCAN S8000G Raman FIB-SEM ($CeMoN$) with a final ion-beam cleaning at 2 kV to minimize surface amorphization.

X-ray fluorescence (XRF) measurements were carried out using a Fischer XDD XRF to map compositions across sample libraries, with a particular emphasis on cation ratio and to estimate the thickness of the films. Light elements (N and O) were analyzed using Auger emission spectroscopy (AES) on a PHI electronics AES 680

nanoprobe with a 5 kV/20 nA defocused electron beam such that a circular area 50 μm in diameter was probed. Between measurement cycles, ion milling was performed using a 3 kV atomic argon beam. Compositions of samples imaged with transmission electron microscopy (TEM) were also confirmed via EDS.

Magnetic properties were measured via superconducting quantum interference device (SQUID) magnetometry in a Quantum Design Magnetic Properties Measurement System (MPMS3). The films were measured from 1.8 to 300 K under applied fields from -7 to $+7$ T. To isolate the signal of the films, bare substrates were also measured and subtracted. The substrates used were p-doped Si for $CeWN_3$ and p-doped Si with a thin film of metallic Mo on the back for $CeMoN_3$. The measured $CeWN_3$ film was ~ 150 – 200 nm thick, and the measured $CeMoN_3$ film was ~ 800 – 1000 nm thick.

RESULTS AND DISCUSSION

High-Throughput Computational and Experimental Screening. Potential ABN_3 perovskite nitrides were identified using a tiered screening approach. In the first step, we specified 39 cations that could sit on the A or B sites, yielding 741 candidate ABN_3 compositions. For each of these formulas, we applied three descriptors to assess their viability in the perovskite crystal structure—Goldschmidt's tolerance factor, t , the octahedral factor, μ , and a recently introduced tolerance factor, τ .^{31,32} Using these descriptors, we identified 9 ABN_3 compositions that are likely to crystallize in perovskite structures on the basis of the following criteria: charge-balanced, $0.8 < t < 1$, $\mu > 0.38$, and $P(\tau) > 0.5$, where $P(\tau)$ is the calibrated probability of forming perovskite given τ .³¹ We applied a series of descriptors primarily because τ has not been thoroughly benchmarked on nitrides. The 9 compositions predicted to be stable as perovskites using these criteria are listed in [Table 1](#) along with thermodynamic and electronic properties as calculated with PBE.³⁸ Eight out of 9 of the descriptor-predicted perovskites are also calculated to be thermodynamically stable with respect to competing phases ($\Delta H_d < 0$), supporting the use of these descriptors for nitride perovskites. The one exception, $InMoN_3$, notably has the lowest $P(\tau)$ of the 9 compounds. $LaWN_3$, which is predicted and calculated to be thermodynamically stable in this work, was successfully synthesized in a recent report.¹⁷ A recent computational study also reports the stabilities of $CeTaN_3$, $CeNbN_3$, $CeWN_3$, and $CeMoN_3$ in perovskite structures.⁶

From this evaluation, the compounds $LaWN_3$, $LaMoN_3$, $CeWN_3$, $CeMoN_3$, YWN_3 , and $YMoN_3$ were prioritized for experimental testing because of their calculated stabilities ($\Delta H_d < 0$) and to provide variety across both A- and B-site cations; it should be noted that perovskite $LaWN_3$ has already

been successfully synthesized¹⁷ and was included here for validation purposes.

We attempted to synthesize these six compositions via combinatorial RF cosputtering of metallic targets with the substrate at ambient chamber temperature. The depositions were carried out in ultrahigh vacuum to minimize oxygen contamination. Figure S1 in the [Supporting Information](#) shows the diffraction patterns from these initial screening studies. Diffraction from the (Y,Mo)N and (Y,W)N sample libraries showed clear diffraction peaks only from the AlN capping layer. Despite the AlN capping layer, (La,Mo)N sample libraries oxidized and visibly degraded in a matter of 24–48 h of air exposure, greatly complicating detailed investigation. (Ce,Mo)N and (Ce,W)N sample libraries exhibited clear diffraction peaks and showed no visible evidence of degradation after growth; therefore, these compositions were prioritized for further investigation.

Closer examination of the diffraction patterns from Ce-containing compositions showed two distinct phases with lattice parameters close to those predicted for the perovskite phase (Figure 1). One phase matches diffraction peaks predicted for a perovskite, though the peaks are far too broad to confidently refine the exact symmetry of this phase and therefore are labeled according to pseudocubic axes. The other phase coexisting at the 1:1 A:B cation stoichiometry and Ce-rich compositions for both systems can be matched to a fluorite structure.

To investigate the relative stabilities of phases in the Ce–Mo–N and Ce–W–N phase spaces and to complement the promising experimental results for synthesizing Ce-based perovskites, we expanded our computational analysis of CeMoN₃ and CeWN₃. We recomputed the ternary Ce–Mo–N and Ce–W–N phase diagrams using the r2SCAN meta-GGA density functional⁴³ with additional sampling of potential crystal structures for CeMoN₃ and CeWN₃ and potential competing phases in the Ce–N, Mo–N, and W–N chemical spaces. The computed ternary phase diagrams for these systems are shown in Figure 2 and further support the thermodynamic stability of CeMoN₃ ($\Delta H_d = -178$ meV/atom) and CeWN₃ ($\Delta H_d = -284$ meV/atom) in the orthorhombic perovskite structure (*Pmc2₁*). No fluorite or fluorite-related phase was represented in either phase diagram, although several fluorite-structured CeN_{2–x} phases were considered. Ce₄N₇ was shown to be stable in the fluorite

structure, and Ce₂N₃ was shown to be very nearly stable ($\Delta H_d = +2$ meV/atom). It is possible that ternary fluorites could be stable or nearly stable (similar to those identified in refs 48 and 49), but these were not considered as it is difficult to resolve the stoichiometry in the fluorite phase. This strongly suggests that the fluorite-family phase observed experimentally here is not the thermodynamic equilibrium phase for stoichiometric CeWN₃ or CeMoN₃.

Fluorite phases are famously tolerant to large concentrations of point defects and cation disorder, and they are often encountered as competing phases with Pb-based perovskites such as lead zirconate titanate (PZT) and lead magnesium niobate (PMN)-based piezoelectrics.⁵⁰ Both Pb-rich PZT and Pb-deficient PZT—and even kinetically limited cation-disordered stoichiometric PZT—derived from chemical solutions have been shown to favor crystallization in a fluorite (or pyrochlore, in this case simply an ordered derivative of the fluorite) phase at modest temperatures en route to the stable perovskite phase.^{51,52} It has also been shown that it is possible to convert fluorite phases to perovskite phases with adequate heating in such systems, provided that the stoichiometry is preserved or corrected.^{52,53} Following the successful navigation of the fluorite–perovskite landscape in PZT and the computational guidance that the perovskite phase is lower energy for these targeted stoichiometric chemistries, it should be possible to fabricate single phase nitride perovskites by either immediately accessing the thermodynamically stable phase (e.g., at high temperature) or by adding energy (annealing) and progressively monitoring the phase evolution from mixed fluorite+perovskite to single phase perovskite.

Crystallization Dynamics of CeMoN_{3–x}. Initial (Ce,Mo)-N_{3–x} XRD patterns (Figure 1A) showed two phases present. Postdeposition annealing was performed to encourage crystallization of the thermodynamically stable phase. Extended anneals at 1173 K in flowing N₂ of the initially mixed-phase (perovskite + fluorite) (Ce,Mo)N_{3–x} film grown at 900 K gradually increased the phase fraction of the perovskite phase at the expense of the fluorite (Figure 3A).

To investigate whether this structural evolution may be due to oxidation during annealing, Auger emission spectroscopy (AES) was performed. Shown in Figure 4B, it indicates very low oxygen content through the thickness of the annealed film, confirming the synthesis of an oxygen-free nitride perovskite phase. This goal has proven to be a significant synthetic challenge. Prior to the current work, only two oxygen-free nitride perovskites have been reported, one via high pressure–high temperature methods to synthesize LaReN₃ in bulk¹⁸ and our prior work that used activated nitrogen via a RF plasma to form LaWN₃.¹⁷ The low oxygen content confirms that the 1173 K anneal in flowing N₂ did not cause this fluorite-to-perovskite transition through the inadvertent introduction of oxygen. We therefore conclude that the phenomenon observed in CeMoN_{3–x} films is similar to that previously documented for the PZT system. While the ground state structure is perovskite (Table 1), significant disorder favors crystallization first into a defect- and disorder-tolerant fluorite phase, which can then transform into the stable perovskite after annealing. As shown previously for PZT, the gradual nature of this transition is enabled by the similarity of the perovskite (101) and fluorite (pyrochlore) (222) planes;⁵³ we presume an analogous scenario here.

A LaBail fit of the lab XRD data of a spot with composition Ce_{0.61}Mo_{0.39}N_{3–x} to a pseudocubic perovskite structure with

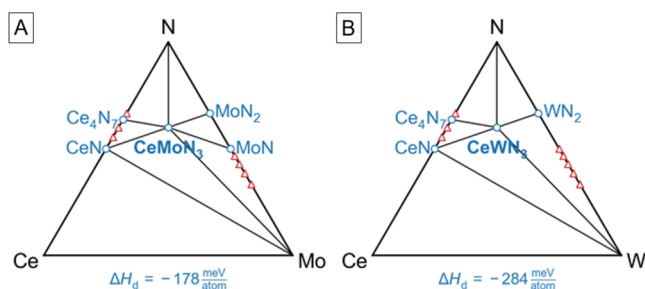


Figure 2. Computed ternary phase diagrams for CeMoN₃ (A) and CeWN₃ (B) showing possible competing phases for each chemistry studied. ΔH_d is shown for the stability-defining reaction for each perovskite phase: $(1/4)\text{Ce}_4\text{N}_7 + (3/4)\text{MoN} + (1/4)\text{MoN}_2 \rightarrow \text{CeMoN}_3$ and $\text{CeN} + \text{WN}_2 \rightarrow \text{CeWN}_3$. Blue circles indicate thermodynamically stable phases, and red triangles indicate thermodynamically unstable phases.

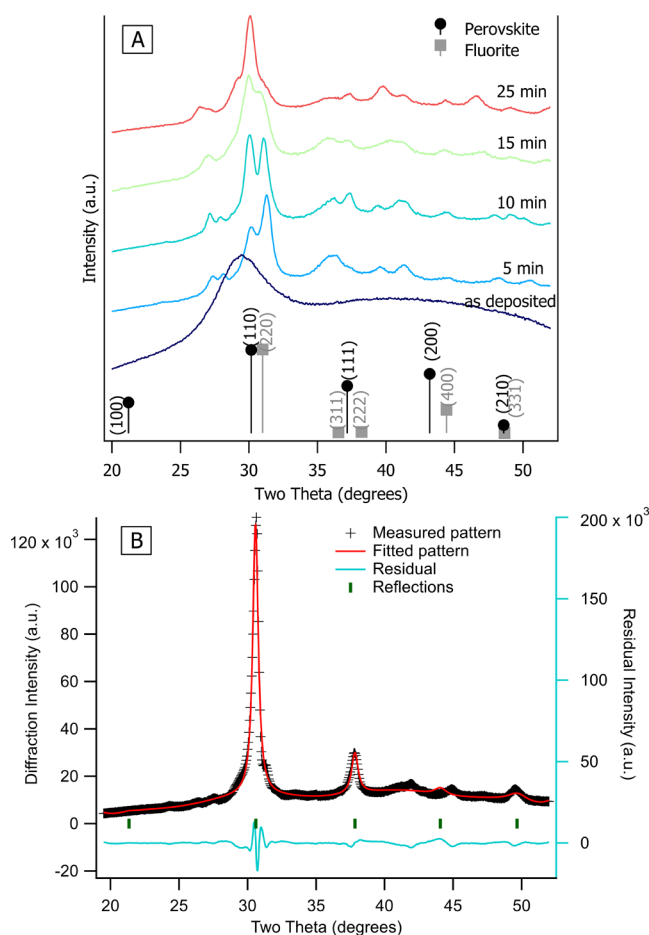


Figure 3. (A) Lab XRD of a single point on a $(\text{Ce},\text{Mo})\text{N}_{3-x}$ film with nominal composition $\text{Ce}_{0.66}\text{Mo}_{0.34}\text{N}_{3-x}$ by XRF annealed at 1173 K for progressive holds in a flowing N_2 atmosphere. A vertical offset is applied to separate the data. (B) LeBail fit in space group $Pm\bar{3}m$ of lab XRD data of the same $(\text{Ce},\text{Mo})\text{N}_{3-x}$ film with nominal composition $\text{Ce}_{0.61}\text{Mo}_{0.39}\text{N}_{3-x}$ annealed at 1173 K for 10 min. $wR = 8.68\%$, and goodness of fit (GOF) = 10.32.

$Pm\bar{3}m$ symmetry is shown in Figure 3B. The extracted lattice parameter was $a = 4.0668(7)$ Å. It is likely that the true symmetry is lower given the presence of several unaccounted for by this cubic space group and given the theoretical calculations that predicted orthorhombic $Pmc2_1$ symmetry with lattice parameters $a = 5.50528$ Å, $b = 5.59140$ Å, and $c = 7.85589$ Å (see Table S3 in the Supporting Information). Determination of the precise space group from the experimental data was hindered by the weak nature of the additional peaks and the broad nature of thin film diffraction peaks.

Direct Growth of Perovskite CeWN_{3-x} . Initial results in the $(\text{Ce},\text{W})\text{N}$ family (Figure 1B)—deposited at ambient temperature followed by 1 min of annealing in N_2 at 1173 K—also revealed an initial mixture of perovskite and fluorite phases near and above the 1:1 cation ratio, but annealing CeWN_{3-x} films with a 1:1 Ce:W ratio at 1173 K in N_2 —analogous to the conditions that produced the perovskite phase in CeMoN_{3-x} —yielded W metal or film delamination. Increasing the substrate temperature to ~ 900 K (the maximum capability of the chamber) during growth yielded perovskite films without evidence of a coexisting fluorite phase, as shown in Figure 5A. There appears to be some effect of texturing for the highest

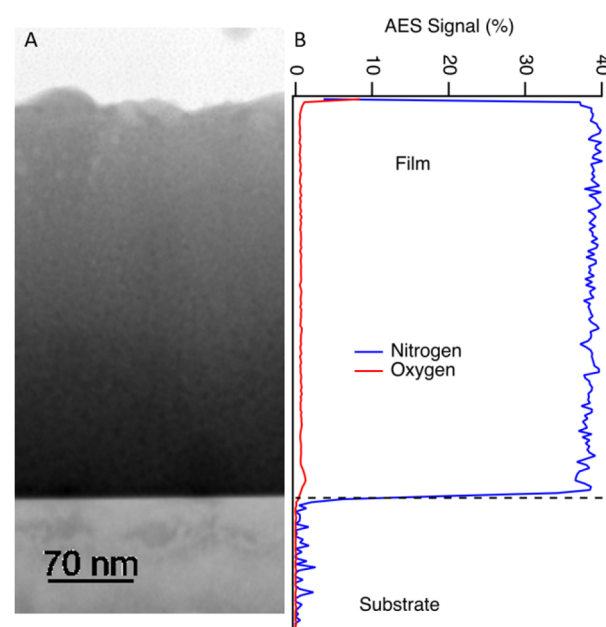


Figure 4. (A) BF STEM cross section showing a very fine grain size and (B) AES depth profile of light element signals of a CeMoN_{3-x} film with nominal composition $\text{Ce}_{0.54}\text{Mo}_{0.46}\text{N}_{3-x}$ by XRF after annealing for 10 min in flowing N_2 . Only the surface layer of the sample contains significant oxygen; the majority of the sample has very low oxygen signal, indicating that the change during annealing is not due to incorporation of oxygen but to crystallization kinetics.

Ce-containing compositions, as the most Ce-rich composition detected showed only a very strong perovskite pseudocubic (110) peak. Comparison of lab X-ray, synchrotron X-ray diffraction (SXRD), and electron diffraction (TEM SAED) data confirms that assignment of a perovskite structure to this phase is appropriate across both long-range (X-ray) and short-range (electron) diffraction lengths (see Figure S2 in the Supporting Information). However, determination of a specific space group is hindered by the small number of peaks present in the phase-pure films. We therefore performed a Le Bail fit to the pseudocubic perovskite structure in space group $Pm\bar{3}m$, shown in Figure 5B for the composition $\text{Ce}_{0.5}\text{W}_{0.5}\text{N}_{3-x}$. The extracted lattice parameter is $a = 4.020(4)$ Å. We note that the pseudocubic symmetry used in the LeBail refinement is different from the theoretically predicted cell in orthorhombic $Pmc2_1$ symmetry with lattice parameters $a = 5.5370$ Å, $b = 5.60061$ Å, and $c = 7.88645$ Å.

In bright field (BF) TEM images, the CeWN_{3-x} films show columnar grains and a dense microstructure (Figure 6A). The columnar grains indicate that crystallization occurred early in the growth, and the established crystals continued to grow, unlike in the above CeMoN_{3-x} microstructure that was amorphous during growth and crystallized during postgrowth annealing steps, leading to the lack of columns in the TEM in Figure 4A. AES results (Figure 6B) show much higher oxygen content for these films than for their CeMoN_{3-x} counterparts (Figure 4B). This sample experienced significant air exposure between growth and the AES measurement, so it is unknown what fraction of the oxygen content was incorporated during growth. The fact that the oxygen to nitrogen ratio measured by AES decreases through the film toward the substrate suggests that some or all of this oxidation occurred after growth. We therefore consider the 2.5:1 nitrogen:oxygen ratio closest to

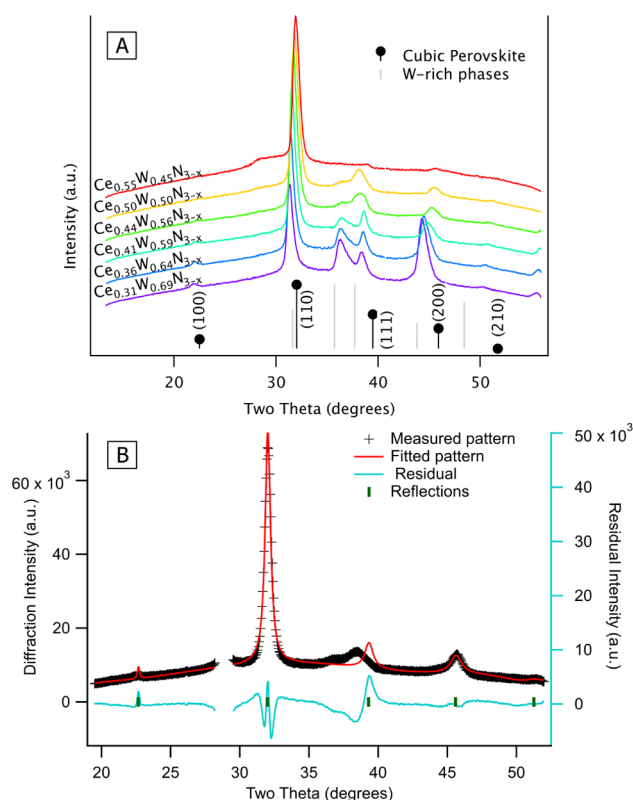


Figure 5. (A) Lab XRD of (Ce,W)N films grown at 900 K showing a phase-pure perovskite near and slightly above the 1:1 Ce:W ratio. At compositions with lower Ce content, W-rich phases formed. A peak associated with the substrate has been removed by removing a range of χ from the integration after it did not appear in electron diffraction in Figure S2 in the [Supporting Information](#). (B) LeBail fit in space group $Pm\bar{3}m$ of the lab XRD pattern of the composition $Ce_{0.5}W_{0.5}N_{3-x}$ in panel A. The 2θ region around a peak associated with the Si substrate has been removed. $wR = 9.38\%$, and goodness of fit (GOF) = 9.85.

the substrate to be a ceiling on the amount of oxygen incorporated during growth, though it is likely that the as-grown films had much less oxygen.

Growth Summary. The above crystallization pathways of (1) postdeposition annealing and (2) high substrate temperature during deposition demonstrate the challenges and flexibility of fabricating new nitride perovskites. In $CeMoN_{3-x}$, the direct growth of the single-phase perovskite was not achieved because the fluorite structure appears to be more kinetically accessible than the perovskite for stoichiometries with a 1:1 Ce:Mo ratio. However, it was possible to access the thermodynamically stable perovskite after annealing. In $CeWN_{3-x}$, the direct growth of perovskite was achieved using the hottest substrate temperature possible in the chamber (~ 900 K) to access the thermodynamically stable perovskite, but postprocessing annealing in a flowing nitrogen chamber induced reduction to W metal. For comparison, the recently reported nitride perovskite $LaWN_3$ ¹⁷ was achieved both with a high substrate temperature during initial sputtering and by postdeposition annealing. These growth pathways can serve as blueprints for accessing more nitride perovskite compounds in the yet-unexplored chemical space.

Magnetic Ground State Calculations. As a result of the presence of unpaired electrons (either f^1 Ce^{3+} or d^1 W^{5+}/Mo^{5+})

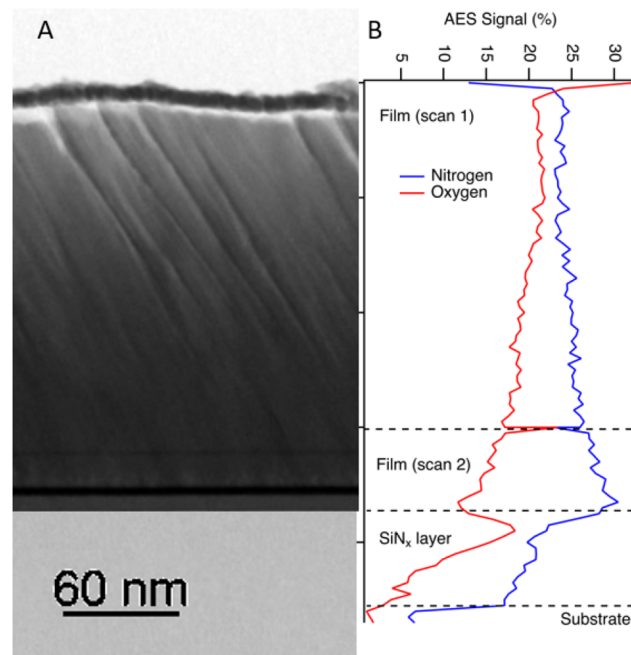


Figure 6. (A) BF STEM cross section of a $CeWN_{3-x}$ film with nominal composition $Ce_{0.51}W_{0.49}N_{3-x}$ by XRF showing columnar microstructure within the film. The dark layer at the top is Pt from sample preparation. (B) AES of the same $CeWN_{3-x}$ film showing increasing oxygen content near the surface of the film, presumably because of prolonged exposure to oxygen in the atmosphere. Two scans were performed as the first did not penetrate the full film depth, which caused a spike in oxygen measured at the newly created surface.

in stoichiometric $CeMN_{3-x}$, there is the possibility for long-range magnetic order in these systems. We calculated the magnetic ground states of $CeMoN_3$ and $CeWN_3$, as shown in [Table 2](#), using the *r2SCAN* functional and orthorhombic $Pmc2_1$ unit cells (see [Table S3](#) in the [Supporting Information](#) for atomic positions and lattice parameters). Three initial configurations were considered for each compound: a ferromagnetic configuration (“FM”) in which moments of $+5 \mu_B$ were placed on all Ce and M, and two different antiferromagnetic configurations (“AFM-1” and “AFM-2”) in which each Ce or M had a moment of either $+5 \mu_B$ or $-5 \mu_B$; these two are different in terms of how the up and down spins are distributed. The optimized net moments for the Ce and M sublattices and the optimized overall net moments resulting from each initial configuration are shown in [Table 2](#). The calculated magnetic moments for each Ce and M site are shown in [Table S4](#) in the [Supporting Information](#).

The ground states and optimized magnetic moments ([Table S4](#) in the [Supporting Information](#)) suggest FM ordering for $CeMoN_3$ with a small net moment of $\sim 0.4 \mu_B$. The presence of net moments on both Ce and Mo sublattices implies that the existence of potentially mixed oxidation states for both metals (Ce^{3+}/Ce^{4+} , Mo^{6+}/Mo^{5+}). However, both AFM configurations are very close in energy to the FM ground state. For $CeWN_3$, the calculated ground state (“AFM-2”) contains ferrimagnetic ordering of the Ce sites (see [Table S4](#) in the [Supporting Information](#)) and no significant moment on any W, yielding a very small net moment of $\sim 0.2 \mu_B$. The other configurations are quite close in energy. Flores-Livas et al. calculated $CeWN_3$ in *Pnma* symmetry to be weakly FM⁸ using a lower level of theory (LDA), considering only Ce, but also accounting for

Table 2. Magnetic Ground-State Calculations for Orthorhombic CeMoN₃ and CeWN₃ Performed with r2SCAN^a

formula	initial configuration	total energy (eV/atom)	net Ce moment (μ_B)	net M moment (μ_B)	net moment (μ_B)	ΔE_{gs} (meV/atom)
CeMoN ₃	FM	−18.0105	−0.25	−0.136	−0.386	0
	AFM-1	−18.0104	−0.001	0	−0.001	0.0945
	AFM-2	−18.0105	0.006	0.004	0.01	0.0505
CeWN ₃	FM	−23.1576	0.456	0.02	0.476	2.3705
	AFM-1	−23.1590	−0.004	−0.002	−0.006	0.9115
	AFM-2	−23.1600	0.201	−0.022	0.179	0

^a ΔE_{gs} is the energy of that magnetic configuration above the lowest energy magnetic configuration considered. FM = initial high-spin ferromagnetic ordering. AFM = initial high-spin anti-ferromagnetic ordering. AFM-1 and AFM-2 differ in the arrangement of positive and negative spins. *M* refers to either Mo or W.

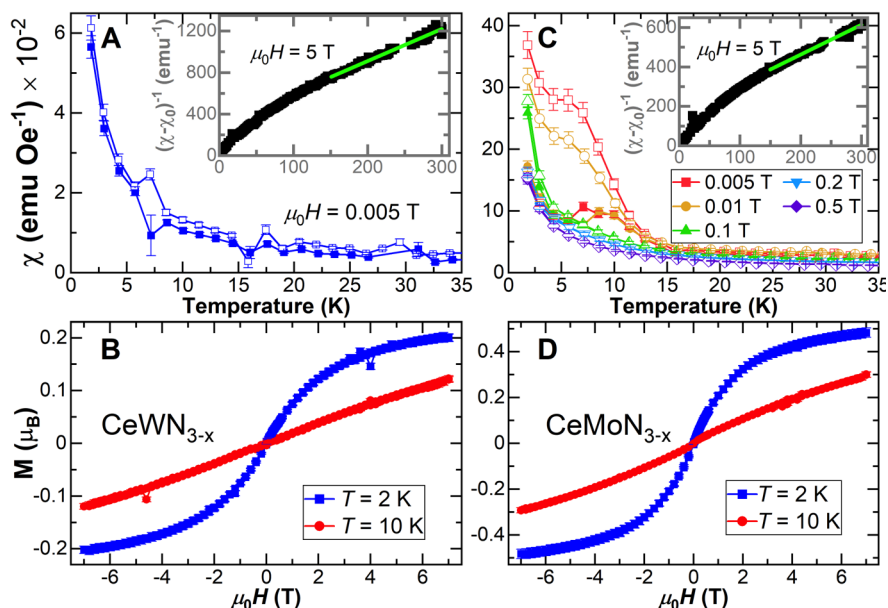


Figure 7. Magnetic properties of CeWN_{3-x} and CeMoN_{3-x}. (A) Low-field zero field cooled (ZFC) and field cooled (FC) susceptibility of CeWN_{3-x} measured in an applied field of $\mu_0 H = 0.005$ T. Inset: Inverse susceptibility measured in an applied field of $\mu_0 H = 5$ T with a diamagnetic correction of $\chi_0 = -3.91 \times 10^{-4}$ emu/Oe. Data in the range $T = 237$ – 256 K are masked out because of instrumental artifacts. The line is a Curie–Weiss fit from $T = 150$ to $T = 300$ K. (B) Magnetization of CeWN_{3-x} as a function of applied field at $T = 2$ K and $T = 10$ K. (C) Low-field ZFC and FC susceptibility of CeMoN_{3-x} measured in applied fields of $\mu_0 H = 0.005$ – 0.5 T. Inset: Inverse susceptibility measured in an applied field of $\mu_0 H = 5$ T with a diamagnetic correction of $\chi_0 = -4.33 \times 10^{-4}$ emu/Oe. Data in the range $T = 238$ – 263 K are masked out because of instrumental artifacts. The line is a Curie–Weiss fit from $T = 150$ to $T = 300$ K. (D) Magnetization of CeMoN_{3-x} as a function of applied field at $T = 2$ K and $T = 10$ K.

spin–orbit coupling. Our higher level r2SCAN calculations performed on a larger unit cell are not necessarily inconsistent with these prior results, as both calculations yielded a net moment, and we show the energy difference between different magnetic configurations is quite small.

Magnetic Susceptibility Measurements. To compare with the calculated magnetic ground states, we performed magnetic susceptibility measurements on perovskite CeWN_{3-x} and CeMoN_{3-x}. Bare substrates were also measured and subtracted in order to isolate the signal from the perovskite phases. As the mass of the perovskite thin film cannot be quantified precisely, we show the data either as magnetization (M , in μ_B) or as susceptibility (χ , in emu/Oe) calculated with an assumed sample mass of 0.0001 g; these values are thus approximate and therefore cannot be accurately compared across samples or used to extract meaningful effective moments (μ_{eff} in μ_B) or Curie constant (C , in K emu/mol) values from the Curie–Weiss fits. We also note that both films may have some amorphous/nanocrystalline phase fraction in addition to the crystalline perovskite phase; this is not easily separable in

the susceptibility data and could complicate the extraction of quantitative susceptibility and effective moment values.

Low-field ($\mu_0 H = 0.005$ T) zero field cooled (ZFC) and field cooled (FC) DC susceptibility measurements were performed on a phase-pure perovskite CeWN_{3-x} film with approximate composition Ce_{0.51}W_{0.49}N_{3-x} measured by XRF (Figure 7A). No indications of long-range magnetic ordering or bifurcation beyond error between the ZFC and the FC scans are observed, indicating overall paramagnetism. Magnetization as a function of applied field (Figure 7B) confirms this behavior: no hysteresis loop or net moment is visible at either $T = 2$ K or $T = 10$ K. However, the change in slope between these two temperatures suggests the presence of short-range correlations. To probe this, a Curie–Weiss fit was performed on high temperature ($T = 150$ – 300 K) inverse susceptibility data collected at $\mu_0 H = 5$ T (Figure 7A, inset). The negative extracted Weiss temperature $\theta = -95(4)$ K indicates the presence of strong antiferromagnetic (AFM) interactions. This suggests the presence of geometric magnetic frustration, an intriguing possibility in this new material, and one that is

relatively common in (double) perovskite oxides and oxynitrides.^{54–56}

Analogous low-field ZFC and FC measurements collected on a CeMoN_{3-x} film with approximate composition $\text{Ce}_{0.61}\text{Mo}_{0.39}\text{N}_{3-x}$ chosen for strong perovskite diffraction peaks, display bifurcation below $T \sim 10$ K and a peak at $T_N \sim 8$ K, which we assign as a transition to long-range AFM order (Figure 7C). This splitting closes as the applied field is increased, and no splitting is observed above $\mu_0 H \sim 0.2$ T. The magnetization as a function of applied field (Figure 7D) at $T = 2$ K is consistent with AFM order. At $T = 10$ K, the magnetization is linear, as expected in the paramagnetic state. A Curie–Weiss fit performed on high temperature ($T = 150$ – 300 K) inverse susceptibility data collected at $\mu_0 H = 5$ T (Figure 7C, inset) yields a negative Weiss temperature $\theta = -106(3)$ K, confirming the dominance of AFM correlations in this material. The frustration index f , which quantifies the magnetic frustration as the ratio between the Weiss temperature and the Néel transition temperature ($f = \left| \frac{\theta}{T_N} \right|$), is approximately 13, indicating a very high degree of frustration.⁵⁷ The upturn below T_N may be attributed to the highly frustrated nature of this compound and/or to a possibly paramagnetic amorphous phase fraction.

While both CeWN_{3-x} and CeMoN_{3-x} show signs of strong short-range AFM correlations as evidenced by their large, negative Weiss temperatures, CeWN_{3-x} remains paramagnetic down to the lowest temperature measured while CeMoN_{3-x} has a transition to long-range AFM order at $T_N \sim 8$ K. This suggests the energy scale of the magnetic interactions is different in these two compounds, most likely because of the difference in spin–orbit coupling between W and Mo. However, subtle differences in structure, stoichiometry, and coupling between the A- and B-site sublattices—or a combination of several effects—may also have a large influence upon the magnetism and must be studied further.

The optimized magnetic moments from our calculations of the orthorhombic perovskites at the r2SCAN level of theory suggest AFM Ce^{3+} and $d^0 \text{W}^{6+}$ for CeWN_3 —consistent with the short-range AFM correlations we extract from the Curie–Weiss fits, although we observe a paramagnetic ground state—but FM ordering and potentially mixed oxidation states ($\text{Ce}^{3+}/\text{Ce}^{4+}$, $\text{Mo}^{6+}/\text{Mo}^{5+}$) for CeMoN_3 . However, the calculated AFM configurations for CeMoN_3 are very close in energy to the FM ground state, and therefore the observed AFM behavior may easily be stabilized.

The origin of the observed magnetic behavior will be the focus of further detailed study, as the background subtraction of substrates and the uncertainty in film mass complicate the accurate extraction of magnetization and μ_{eff} values, which are ideally able to distinguish between $S = 1/2 \text{W}^{5+}/\text{Mo}^{5+}$ ($\mu_{\text{eff}} = 1.73 \mu_B$) and $J = 5/2 \text{Ce}^{3+}$ ($\mu_{\text{eff}} = 2.54 \mu_B$). Both simple pictures— $f^1 \text{Ce}^{3+}$ or $d^1 \text{W}^{5+}/\text{Mo}^{5+}$ —are possible because AFM correlations are common in both. While most rare earth elements often display ferromagnetic (FM) correlations, Ce^{3+} cations are affected by two competing interactions: indirect exchange mediated by conduction electrons (i.e., the RKKY interaction),^{58,59} which generally stabilizes the AFM order,^{60–63} and Kondo screening, which leads to a non-magnetic ground state.^{64,65} Only occasionally is a FM ground state observed, either via an itinerant mechanism or arising at very low temperatures in fierce competition with AFM order.^{66,67} However, the possibility of Ce in a mixed $+3/+4$

valence state, which typically carries no stable magnetic moment, must also be considered; this is reported to be the ground state of CeN.⁶⁸ Future work incorporating other magnetic transition metals (TMs)—such as $3d$ TMs (e.g., Fe, Co, Mn, ...) or $4d/5d$ TMs (e.g., Re, Ir, Ru, ...) that often cause useful or exotic magnetism in oxide perovskites—would be intriguing but may be difficult given charge balance requirements for nitride perovskites. Several of these TMs were probed computationally in this study (Nb, Ta, Cr, Mn, Fe, Co, Ni), but the cutoffs for $P(\tau)$, t , or μ were not met in the screening section (see the High-Throughput Computational and Experimental Screening section above and Table S1 in the Supporting Information).

CONCLUSIONS

In this study, two new compositions of nitride perovskites have been experimentally realized. Candidate compositions were first filtered using radii-based descriptors and DFT calculations of thermodynamic stability, then through high-throughput experimental growths before efforts were focused on CeMoN_3 and CeWN_3 for further study. Initial films of compositions both grown at ambient temperature and annealed at elevated temperature exhibited a perovskite and a coexisting phase that is hypothesized to be in the fluorite family. Similar to what is seen in the PZT system, the fluorite phase appears to be a transient intermediate phase that is present during crystallization from amorphous material to a more stable perovskite phase. For CeMoN_{3-x} films, growth at the maximum substrate temperature achievable in our chamber produced films with a mix of fluorite and perovskite phases, and extended annealing promoted conversion of the fluorite to perovskite. This compound was shown to be oxygen-free, representing only the third known oxygen-free nitride perovskite. With progressive annealing, this phase showed a deviation from the pseudocubic pattern: peak splitting suggested a transition to a lower symmetry, such as the predicted orthorhombic phase. CeWN_{3-x} films grown at this maximum substrate temperature (~ 900 K) were single-phase perovskite as grown. Magnetic susceptibility measurements of these perovskite samples indicate that CeWN_{3-x} is paramagnetic down to $T = 2$ K with strong short-range antiferromagnetic correlations, while CeMoN_{3-x} orders antiferromagnetically at $T_N \approx 8$ K. Both materials show indications of a high degree of magnetic frustration. These observations differ from the previously predicted ferromagnetic behavior,⁸ as well as our current calculations of ferrimagnetic and ferromagnetic ground states for orthorhombic CeWN_3 and CeMoN_3 , respectively. This work clearly demonstrates the value of coupled high-throughput computation and experiment for the discovery and successful realization of new materials and a promising outlook for synthesis of new nitride perovskites.

ASSOCIATED CONTENT

Supporting Information

The Supporting Information is available free of charge at <https://pubs.acs.org/doi/10.1021/acs.chemmater.2c01282>.

Tolerance factor data for all charge-balanced nitride compositions, deposition parameters for experimental screening films, X-ray diffraction of the screening experimental films, additional TEM data, calculated CIFs, and calculations of magnetic ground states (PDF) Crystallographic information file for CeMoN_3 (CIF)

Crystallographic information file for CeWN₃ (CIF)

AUTHOR INFORMATION

Corresponding Authors

Rachel Sherbondy — Materials Science Center, National Renewable Energy Laboratory, Golden, Colorado 80401, United States; Metallurgical and Materials Engineering Department, Colorado School of Mines, Golden, Colorado 80401, United States; orcid.org/0000-0002-1304-4171; Email: rsherbondy@mines.edu

Andriy Zakutayev — Materials Science Center, National Renewable Energy Laboratory, Golden, Colorado 80401, United States; orcid.org/0000-0002-3054-5525; Email: andriy.zakutayev@nrel.gov

Geoff L. Brennecke — Metallurgical and Materials Engineering Department, Colorado School of Mines, Golden, Colorado 80401, United States; orcid.org/0000-0002-4476-7655; Email: gbrennec@mines.edu

Authors

Rebecca W. Smaha — Materials Science Center, National Renewable Energy Laboratory, Golden, Colorado 80401, United States; orcid.org/0000-0002-8349-2615

Christopher J. Bartel — Department of Materials Science and Engineering, University of California, Berkeley, Berkeley, California 94720, United States; orcid.org/0000-0002-5198-5036

Megan E. Holtz — Metallurgical and Materials Engineering Department, Colorado School of Mines, Golden, Colorado 80401, United States

Kevin R. Talley — Materials Science Center, National Renewable Energy Laboratory, Golden, Colorado 80401, United States; Present Address: Qorvo Inc., Bend, Oregon 97701, United States; orcid.org/0000-0003-4575-4140

Ben Levy-Wendt — SLAC National Accelerator Laboratory, Menlo Park, California 94025, United States; Department of Mechanical Engineering, Stanford University, Palo Alto, California 94305, United States

Craig L. Perkins — Materials Science Center, National Renewable Energy Laboratory, Golden, Colorado 80401, United States; orcid.org/0000-0002-9036-8698

Serena Eley — Department of Physics, Colorado School of Mines, Golden, Colorado 80401, United States

Complete contact information is available at:

<https://pubs.acs.org/10.1021/acs.chemmater.2c01282>

Notes

The views expressed in the article do not necessarily represent the views of the DOE or the U.S. Government.

The authors declare no competing financial interest.

ACKNOWLEDGMENTS

This work was authored in part at the National Renewable Energy Laboratory, operated by Alliance for Sustainable Energy, LLC, for the U.S. Department of Energy (DOE) under Contract No. DE-AC36-08GO28308. Funding was provided by the Office of Science (SC), Basic Energy Sciences (BES), Materials Chemistry program, as a part of the Early Career Award “Kinetic Synthesis of Metastable Nitrides” (synthesis) and by the National Science Foundation (NSF) through Grants No. DMR-1555015 and DMREF-1534503 (characterization). The TESCAN S800G FIB-SEM used in

this work was acquired through the support of the National Science Foundation (DMR-1828454). The MPMS3 measurement system used was acquired through NSF MRI Grant No. 1917860. Use of the Stanford Synchrotron Radiation Light-source, SLAC National Accelerator Laboratory, is supported by the U.S. Department of Energy, Office of Science, Office of Basic Energy Sciences, under Contract No. DE-AC02-76SF00515. This work also used computational resources sponsored by the Department of Energy’s Office of Energy Efficiency and Renewable Energy, located at NREL. R.S. was supported by the NSF Graduate Research Fellowship Program under Grant No. 1646713. R.W.S. acknowledges support from the Director’s Fellowship within NREL’s Laboratory Directed Research and Development program. The authors thank A.M. Holder for useful discussions.

REFERENCES

- (1) Sun, W.; Bartel, C. J.; Arca, E.; Bauers, S. R.; Matthews, B.; Orvañanos, B.; Chen, B. R.; Toney, M. F.; Schelhas, L. T.; Tumas, W.; Tate, J.; Zakutayev, A.; Lany, S.; Holder, A. M.; Ceder, G. A map of the inorganic ternary metal nitrides. *Nat. Mater.* **2019**, *18*, 732–739.
- (2) Zakutayev, A.; Bauers, S. R.; Lany, S. Experimental Synthesis of Theoretically Predicted Multivalent Ternary Nitride Materials. *Chem. Mater.* **2022**, *34*, 1418–1438.
- (3) Matar, S. F.; Demazeau, G. Potential existence of post-perovskite nitrides; DFT studies of ThTa₃N₃. *J. Solid State Chem.* **2010**, *183*, 994–999.
- (4) Sarmiento-Pérez, R.; Cerqueira, T. F. T.; Körbel, S.; Botti, S.; Marques, M. A. L. Prediction of Stable Nitride Perovskites. *Chem. Mater.* **2015**, *27*, 5957–5963.
- (5) Jung, M.-C.; Lee, K.-W.; Pickett, W. E. Perovskite ThTa₃N₃: A large-thermopower topological crystalline insulator. *Phys. Rev. B* **2018**, *97*, 121104.
- (6) Ha, V.-a.; Lee, H.; Giustino, F. CeTa₃N₃ and CeNb₃N₃: Prospective Nitride Perovskites with Optimal Photovoltaic Band Gaps. *Chem. Mater.* **2022**, *34*, 2107–2122.
- (7) Fang, Y.-W.; Fisher, C. A. J.; Kuwabara, A.; Shen, X.-W.; Ogawa, T.; Moriwake, H.; Huang, R.; Duan, C.-G. Lattice dynamics and ferroelectric properties of the nitride perovskite LaWN₃. *Phys. Rev. B* **2017**, *95*, 014111.
- (8) Flores-Livas, J. A.; Sarmiento-Pérez, R.; Botti, S.; Goedecker, S.; Marques, M. A. L. Rare-earth magnetic nitride perovskites. *Journal of Physics: Materials* **2019**, *2*, 025003.
- (9) Bacher, P.; Antoine, P.; Marchand, R.; L’Haridon, P.; Laurent, Y.; Roult, G. Time-of-flight neutron diffraction study of the structure of the perovskite-type oxynitride LaWO_{0.6}N_{2.4}. *J. Solid State Chem.* **1988**, *77*, 67–71.
- (10) Brese, N. E.; DiSalvo, F. Synthesis of the First Thorium-Containing Nitride Perovskite, TaThN₃. *J. Solid State Chem.* **1995**, *120*, 378–380.
- (11) Clarke, S. J.; Guinot, B. P.; Michie, C. W.; Calmont, M. J.; Rosseinsky, M. J. Oxynitride perovskites: Synthesis and structures of LaZrO₂N, NdTiO₂N, and LaTiO₂N and comparison with oxide perovskites. *Chem. Mater.* **2002**, *14*, 288–294.
- (12) Yang, M.; Oró-Solé, J.; Kusmartseva, A.; Fuertes, A.; Attfield, J. P. Electronic tuning of two metals and colossal magnetoresistances in EuWO_{1+x}N_{2–x} perovskites. *J. Am. Chem. Soc.* **2010**, *132*, 4822–4829.
- (13) Fuertes, A. Chemistry and applications of oxynitride perovskites. *J. Mater. Chem.* **2012**, *22*, 3293–3299.
- (14) Black, A. P.; Johnston, H. E.; Oró-Solé, J.; Bozzo, B.; Ritter, C.; Frontera, C.; Attfield, J. P.; Fuertes, A. Nitride tuning of lanthanide chromites. *Chem. Commun.* **2016**, *52*, 4317–4320.
- (15) Talley, K. R.; Mangum, J.; Perkins, C. L.; Woods-Robinson, R.; Mehta, A.; Gorman, B. P.; Brennecke, G. L.; Zakutayev, A. Synthesis of Lanthanum Tungsten Oxynitride Perovskite Thin Films. *Adv. Electron. Mater.* **2019**, *5*, 1900214.

- (16) Niewa, R. Metal-Rich Ternary Perovskite Nitrides. *Eur. J. Inorg. Chem.* **2019**, 2019, 3647–3660.
- (17) Talley, K. R.; Perkins, C. L.; Diercks, D. R.; Brennecke, G. L.; Zakutayev, A. Synthesis of LaWN_3 nitride perovskite with polar symmetry. *Science* **2021**, 374, 1488–1491.
- (18) Kloß, S. D.; Weidemann, M. L.; Atfield, J. P. Preparation of Bulk-Phase Nitride Perovskite LaReN_3 and Topotactic Reduction to LaNiO_2 -Type LaReN_2 . *Angew. Chem., Int. Ed.* **2021**, 60, 22260–22264.
- (19) Caskey, C. M.; Richards, R. M.; Ginley, D. S.; Zakutayev, A. Thin film synthesis and properties of copper nitride, a metastable semiconductor. *Mater. Horiz.* **2014**, 1, 424–430.
- (20) Bauers, S. R.; Holder, A.; Sun, W.; Melamed, C. L.; Woods-Robinson, R.; Mangum, J.; Perkins, J.; Tumas, W.; Gorman, B.; Tamboli, A.; Ceder, G.; Lany, S.; Zakutayev, A. Ternary nitride semiconductors in the rocksalt crystal structure. *Proc. Natl. Acad. Sci. U.S.A.* **2019**, 116, 14829–14834.
- (21) Heinselman, K. N.; Lany, S.; Perkins, J. D.; Talley, K. R.; Zakutayev, A. Thin Film Synthesis of Semiconductors in the Mg–Sb–N Materials System. *Chem. Mater.* **2019**, 31, 8717–8724.
- (22) Greenaway, A. L.; Loutris, A. L.; Heinselman, K. N.; Melamed, C. L.; Schnepf, R. R.; Tellekamp, M. B.; Woods-Robinson, R.; Sherbondy, R.; Bardgett, D.; Bauers, S.; Zakutayev, A.; Christensen, S. T.; Lany, S.; Tamboli, A. C. Combinatorial Synthesis of Magnesium Tin Nitride Semiconductors. *J. Am. Chem. Soc.* **2020**, 142, 8421–8430.
- (23) Fioretti, A. N.; Zakutayev, A.; Moutinho, H.; Melamed, C.; Perkins, J. D.; Norman, A. G.; Al-Jassim, M.; Toberer, E. S.; Tamboli, A. C. Combinatorial insights into doping control and transport properties of zinc tin nitride. *J. Mater. Chem. C* **2015**, 3, 11017–11028.
- (24) Manna, S.; Talley, K. R.; Gorai, P.; Mangum, J.; Zakutayev, A.; Brennecke, G. L.; Stevanović, V.; Ciobanu, C. V. Enhanced Piezoelectric Response of AlN via CrN Alloying. *Phys. Rev. Appl.* **2018**, 9, 034026.
- (25) Bikowski, A.; Siol, S.; Gu, J.; Holder, A.; Mangum, J. S.; Gorman, B.; Tumas, W.; Lany, S.; Zakutayev, A. Design of Metastable Tin Titanium Nitride Semiconductor Alloys. *Chem. Mater.* **2017**, 29, 6511–6517.
- (26) Nguyen, H. H.; Oguchi, H.; Van Minh, L.; Kuwano, H. High-throughput investigation of a lead-free AlN-Based piezoelectric material, $(\text{Mg,Hf})_{1-x}\text{Al}_x\text{N}$. *ACS Comb. Sci.* **2017**, 19, 365–369.
- (27) Riedl, A.; Daniel, R.; Todt, J.; Stefanelli, M.; Holec, D.; Sartory, B.; Krywka, C.; Müller, M.; Mitterer, C.; Keckes, J. A combinatorial X-ray sub-micron diffraction study of microstructure, residual stress and phase stability in TiAlN coatings. *Surf. Coat. Technol.* **2014**, 257, 108–113.
- (28) Reeswinkel, T.; Sangiovanni, D. G.; Chirita, V.; Hultman, L.; Schneider, J. M. Structure and mechanical properties of TiAlN-WNx thin films. *Surf. Coat. Technol.* **2011**, 205, 4821–4827.
- (29) Tholander, C.; Tasnádi, F.; Abrikosov, I. A.; Hultman, L.; Birch, J.; Alling, B. Large piezoelectric response of quaternary wurtzite nitride alloys and its physical origin from first principles. *Phys. Rev. B* **2015**, 92, 174119.
- (30) Bauers, S. R.; Mangum, J.; Harvey, S. P.; Perkins, J. D.; Gorman, B.; Zakutayev, A. Epitaxial growth of rock salt MgZrN_2 semiconductors on MgO and GaN. *Appl. Phys. Lett.* **2020**, 116, 102102.
- (31) Bartel, C. J.; Sutton, C.; Goldsmith, B. R.; Ouyang, R.; Musgrave, C. B.; Ghiringhelli, L. M.; Scheffler, M. New tolerance factor to predict the stability of perovskite oxides and halides. *Sci. Adv.* **2019**, 5, eaav0693.
- (32) Goldschmidt, V. M. Die Gesetze der Krystallochemie. *Naturwissenschaften* **1926**, 14, 477–485.
- (33) Shannon, R. D. Revised effective ionic radii and systematic studies of interatomic distances in halides and chalcogenides. *Acta Crystallogr., Sect. A* **1976**, 32, 751–767.
- (34) Dronskowski, R. *Computational Chemistry of Solid State Materials: A Guide for Materials Scientists, Chemists, Physicists and others*; Wiley-VCH Verlag GmbH: 2005.
- (35) Blöchl, P. E. Projector augmented-wave method. *Phys. Rev. B* **1994**, 50, 17953–17979.
- (36) Kresse, G.; Joubert, D. From ultrasoft pseudopotentials to the projector augmented-wave method. *Phys. Rev. B* **1999**, 59, 1758–1775.
- (37) Kresse, G.; Furthmüller, J. Efficient iterative schemes for ab initio total-energy calculations using a plane-wave basis set. *Phys. Rev. B* **1996**, 54, 11169–11186.
- (38) Perdew, J. P.; Burke, K.; Ernzerhof, M. Generalized Gradient Approximation Made Simple. *Phys. Rev. Lett.* **1996**, 77, 3865–3868.
- (39) Jain, A.; Ong, S. P.; Hautier, G.; Chen, W.; Richards, W. D.; Dacek, S.; Cholia, S.; Gunter, D.; Skinner, D.; Ceder, G.; Persson, K. A. Commentary: The Materials Project: A materials genome approach to accelerating materials innovation. *Appl. Phys. Lett. Mater.* **2013**, 1, 011002.
- (40) Bartel, C. J.; Weimer, A. W.; Lany, S.; Musgrave, C. B.; Holder, A. M. The role of decomposition reactions in assessing first-principles predictions of solid stability. *npj Comput. Mater.* **2019**, 5, 4.
- (41) Bartel, C. J. Review of computational approaches to predict the thermodynamic stability of inorganic solids. *J. Mater. Sci.* **2022**, 57, 10475.
- (42) Bartel, C. J.; Clary, J. M.; Sutton, C.; Vigil-Fowler, D.; Goldsmith, B. R.; Holder, A. M.; Musgrave, C. B. Inorganic Halide Double Perovskites with Optoelectronic Properties Modulated by Sublattice Mixing. *J. Am. Chem. Soc.* **2020**, 142, 5135–5145.
- (43) Furness, J. W.; Kaplan, A. D.; Ning, J.; Perdew, J. P.; Sun, J. Accurate and Numerically Efficient r2SCAN Meta-Generalized Gradient Approximation. *J. Phys. Chem. Lett.* **2020**, 11, 8208–8215.
- (44) Talley, K. R.; Bauers, S. R.; Melamed, C. L.; Papac, M. C.; Heinselman, K. N.; Khan, I.; Roberts, D. M.; Jacobson, V.; Mis, A.; Brennecke, G. L.; Perkins, J. D.; Zakutayev, A. COMBIGor: Data-analysis package for combinatorial materials science. *ACS Comb. Sci.* **2019**, 21, 537–547.
- (45) Zakutayev, A.; Wunder, N.; Schwarting, M.; Perkins, J. D.; White, R.; Munch, K.; Tumas, W.; Phillips, C. An open experimental database for exploring inorganic materials. *Sci. Data* **2018**, 5, 180053.
- (46) Talley, K. R.; White, R.; Wunder, N.; Eash, M.; Schwarting, M.; Evenson, D.; Perkins, J. D.; Tumas, W.; Munch, K.; Phillips, C.; Zakutayev, A. Research data infrastructure for high-throughput experimental materials science. *Patterns* **2021**, 2, 100373.
- (47) Toby, B. H.; Von Dreele, R. B. GSAS-II: the genesis of a modern open-source all purpose crystallography software package. *J. Appl. Crystallogr.* **2013**, 46, 544–549.
- (48) Jacobs, H.; Hellmann, B. Synthesis and structure of a caesium niobium(V) nitride, CsNbN_2 . *J. Alloys Compd.* **1993**, 191, 277–278.
- (49) Jacobs, H.; von Pinkowski, E. Synthese ternärer nitride von alkalimetallen: Verbindungen MIT tantal, $\text{MTaN}_2\text{MIT M} \equiv \text{Na, K, Rb und Cs}$. *J. Less-Common Met.* **1989**, 146, 147–160.
- (50) Swartz, S. L.; Shrout, T. R. Fabrication of perovskite lead magnesium niobate. *Mater. Res. Bull.* **1982**, 17, 1245–1250.
- (51) Polli, A. D.; Lange, F. F.; Levi, C. G. Metastability of the Fluorite, Pyrochlore, and Perovskite Structures in the $\text{PbO}–\text{ZrO}_2–\text{TiO}_2$ System. *J. Am. Ceram. Soc.* **2000**, 83, 873–881.
- (52) Brennecke, G. L.; Parish, C. M.; Tuttle, B. A.; Brewer, L. N.; Rodriguez, M. A. Reversibility of the Perovskite-to-Fluorite Phase Transformation in Lead-Based Thin and Ultrathin Films. *Adv. Mater.* **2008**, 20, 1407–1411.
- (53) Voigt, J. A.; Tuttle, B. A.; Headley, T. J.; Lamppa, D. L. The Pyrochlore-to-Perovskite Transformation in Solution-Derived Lead Zirconate Titanate Thin Films. *MRS Online Proc. Library* **1995**, 395–402.
- (54) Vasala, S.; Karppinen, M. $\text{A}_2\text{B}^*\text{B}^*\text{O}_6$ perovskites: A review. *Prog. Solid State Chem.* **2015**, 43, 1–36.
- (55) Fuentes, A. Metal oxynitrides as emerging materials with photocatalytic and electronic properties. *Mater. Horiz.* **2015**, 2, 453–461.

- (56) Ishida, K.; Tassel, C.; Watabe, D.; Takatsu, H.; Brown, C. M.; Nilsen, G. J.; Kageyama, H. Spin Frustration in Double Perovskite Oxides and Oxynitrides: Enhanced Frustration in $\text{La}_2\text{MnTaO}_5\text{N}$ with a Large Octahedral Rotation. *Inorg. Chem.* **2021**, *60*, 8252–8258.
- (57) Ramirez, A. P. Strongly Geometrically Frustrated Magnets. *Annu. Rev. Mater. Sci.* **1994**, *24*, 453–480.
- (58) Ruderman, M. A.; Kittel, C. Indirect Exchange Coupling of Nuclear Magnetic Moments by Conduction Electrons. *Phys. Rev.* **1954**, *96*, 99–102.
- (59) Kasuya, T. A Theory of Metallic Ferro- and Antiferromagnetism on Zener's Model. *Prog. Theor. Phys.* **1956**, *16*, 45–57.
- (60) Rossat-Mignod, J.; Burlet, P.; Quezel, S.; Effantin, J.; Delacôte, D.; Bartholin, H.; Vogt, O.; Ravot, D. Magnetic properties of cerium mononictides. *J. Magn. Magn. Mater.* **1983**, *31–34*, 398–404.
- (61) Fikáček, J.; Prokleška, J.; Prchal, J.; Custers, J.; Sechovský, V. Nature of the magnetic ground state in the mixed valence compound CeRuSn : a single-crystal study. *J. Phys.: Condens. Matter* **2013**, *25*, 416006.
- (62) Pöttgen, R.; Chevalier, B. Cerium intermetallics with ZrNiAl -type structure – a review. *Z. Naturforsch., B* **2015**, *70*, 289–304.
- (63) Porter, S. H.; Huang, Z.; Cheng, Z.; Avdeev, M.; Chen, Z.; Dou, S.; Woodward, P. M. Structural and magnetic properties of RTiNO_2 ($R = \text{Ce, Pr, Nd}$) perovskite nitride oxides. *J. Solid State Chem.* **2015**, *226*, 279–285.
- (64) Kondo, J. Resistance Minimum in Dilute Magnetic Alloys. *Prog. Theor. Phys.* **1964**, *32*, 37–49.
- (65) Galler, A.; Ener, S.; Maccari, F.; Dirba, I.; Skokov, K. P.; Gutfleisch, O.; Biermann, S.; Pourovskii, L. V. Intrinsically weak magnetic anisotropy of cerium in potential hard-magnetic intermetallics. *npj Quantum Mater.* **2021**, *6*, 2.
- (66) Kishimoto, Y.; Kawasaki, Y.; Ohno, T. ^{11}B NMR Study of Magnetism in RRh_3B_2 ($R = \text{La, Ce, Nd, Sm, Eu and Gd}$). *J. Phys. Soc. Jpn.* **2004**, *73*, 1970–1981.
- (67) Prakash, O.; Thamizhavel, A.; Ramakrishnan, S. Ferromagnetic ordering of minority Ce^{3+} spins in a quasi-skutterudite $\text{Ce}_3\text{Os}_4\text{Ge}_{13}$ single crystal. *Phys. Rev. B* **2016**, *93*, 064427.
- (68) Schumacher, D. P.; Wallace, W. E. Magnetic Characteristics of Some Lanthanide Nitrides. *Inorg. Chem.* **1966**, *5*, 1563–1567.